Research Square

Preprints are preliminary reports that have not undergone peer review.
They should not be considered conclusive, used to inform clinical practice,
or referenced by the media as validated information.

Cerium–Selenium Co-Substituted Hydroxyapatite Nanoparticles with Enhanced Biofunctional Performance for Bone Substitute Applications

Asfia Saeed
asfia.scd@stmu.edu.pk

Shifa Tameer-e-Millat University
Aalia Khanem
International Islamic University
Farwa Naqvi
University of Karachi
Maria Khalid
University of Karachi
Farhan Younas
International Islamic University
Almas Jabeen
University of Karachi
Muhammad Nawaz
Imam Abdulrahman Bin Faisal University
Talha Nisar
Constructor University
Veit Wagner
Constructor University
Muhammad Raza Shah
University of Karachi
Ali Haider
Quaid-i-Azam University
Abdul Samad Khan
Imam Abdulrahman Bin Faisal University

Research Article

Keywords: Hydroxyapatite, Ion Substitution, Antioxidant, Anti-inflammatory, Antibacterial, Cytocompatibility

Posted Date: November 3rd, 2026

DOI: https://doi.org/10.21203/rs.3.rs-11287707/v1

License: This work is licensed under a Creative Commons Attribution 4.0 International License.
Read Full License

Additional Declarations: No competing interests reported.

Abstract

Hydroxyapatite (HA) is widely used as a bone substitute; however, its limited intrinsic antimicrobial, antioxidant, and anti-inflammatory activities can constrain its performance in biologically challenging environments. In this study, cerium- and selenium-co-substituted hydroxyapatite (CS-HA) with varying substitution levels was synthesized hydrothermally to develop a multifunctional HA-based biomaterial. Pure HA and single-ion-substituted Ce-HA and Se-HA were prepared as reference materials. Energy-dispersive X-ray spectroscopy (EDX) confirmed the presence of Ce and Se, while X-ray photoelectron spectroscopy (XPS) provided further evidence of their incorporation into the substituted material. Fourier transform infrared spectroscopy (FTIR) and X-ray diffraction (XRD) demonstrated that the hexagonal crystalline structure of HA was preserved following co-substitution. Ce-Se co-substitution decreased the crystallite size and increased the surface area while maintaining moderate to high crystallinity. Biological evaluation revealed dose-dependent antimicrobial, antioxidant, and anti-inflammatory activities. CS-HA nanoparticles exhibited improved antimicrobial activity against Klebsiella pneumoniae, Pseudomonas aeruginosa, and Acinetobacter baumannii. Their antioxidant activity was comparable to Se-HA and higher than that of pure HA and Ce-HA, whereas their anti-inflammatory activity exceeded that of HA and Se-HA. Cytocompatibility evaluation using human gingival fibroblasts (HGF-1) showed ≥70% cell viability under the tested conditions, meeting the cytotoxicity criteria specified in ISO 10993-5. At higher substituent levels, CS-HA also reduced the viability of CAL-27 squamous cell carcinoma cells. These findings demonstrate that Ce-Se co-substitution can modulate the physicochemical and biofunctional properties of HA, supporting further investigation of CS-HA as a multifunctional biomaterial for bone substitute applications and its potential activity against squamous cell carcinoma.

1. Introduction

Hydroxyapatite (HA) is a bioactive, biocompatible, and osteoconductive bioceramic that resembles the inorganic phase of bone and teeth [1]. It is used for bone grafting, implant coatings, dental tissue remineralization, and localized drug-delivery [2]. However, stoichiometric synthetic HA degrades slowly in vivo, has limited mechanical strength, and shows minimal intrinsic antimicrobial and anti-inflammatory activity [3, 4]. These limitations can restrict its performance in dynamic biologically challenging environments, particularly in the oral cavity and infected bone defects, where microbial colonization, inflammation, fluctuating pH, and oxidative stress can compromise tissue healing [5].

Ionic substitution provides an effective strategy for modifying physicochemical and biological properties of HA [6]. Substitution at the calcium (Ca^{2+}) and phosphate (PO_4^{3-}) sites modifies the crystallographic orientation of HA, surface charge and solubility of HA, thereby influencing its biological properties [7]. Therapeutic ions such as magnesium (Mg^{2+}), zinc (Zn^{2+}), silver (Ag^{2+}), and strontium (Sr^{2+}) have been incorporated into HA to support osteogenesis and reduce the risk of post-surgical infection [6].

Cerium (Ce) has gained considerable attention for its dual oxidation states (Ce^{3+}/Ce^{4+}) and reversible redox cycle [8][9]. Under infected conditions, cerium exhibits peroxidase/oxidase activity and reduces

microbial load. In contrast, under normal physiological conditions, it protects against cellular damage by scavenging excess reactive oxygen species (ROS) through superoxide dismutase- and catalase-like activity [8]. In addition, cerium has been shown to modify inflammatory pathways [10]. Cerium-substituted HA (Ce-HA) inhibits oral microbes while promoting proliferation of human periodontal fibroblasts [9, 11].

Selenium, an essential micronutrient, is a key component of selenoproteins and is valued for its antioxidant, immunomodulatory, and anticancer properties [6, 12]. Selenium facilitates bone healing by promoting osteoblastic differentiation, collagen-1 formation, and alkaline phosphatase secretion[6, 13]. Moreover, selenium-doped HA has demonstrated selective toxicity against osteosarcoma cells (MG-63) [14].

Although Ce- and Se-substituted HA have individually demonstrated enhanced biological performance, single-ion substitution may provide a limited range of therapeutic functions in the complex microenvironment of compromised bone healing [15]. The combined effect of cerium-selenium co-substitution remains underexplored. Co-substitution may combine the complementary functions of both ions while modifying the lattice structure, crystallinity and ion-release behavior of HA. However, a detailed investigation of Ce-Se substitution level, physicochemical properties and biological response has not been systematically established.

Therefore, this study aimed to synthesize cerium–selenium co-substituted hydroxyapatite nanoparticles hydrothermally at varying substitution levels. Hydrothermal processing synthesize highly crystalline and homogeneous HA [6]. Pure HA and single-ion-substituted Ce-HA and Se-HA were included as reference materials. By correlating substitution-dependent physicochemical changes with biological responses, this study provides insights into the structure-function relationship of Ce-Se-HA as a multifunctional HA-based material for bone substitute applications. It was hypothesized that varying Ce/SE composition would modify the physicochemical characteristics of HA and therefore would have distinct composition-dependent biological responses.

2. Materials and Methods

The chemical precursors used for the synthesis of nanoparticles included diammonium hydrogen phosphate $\left(\left(NH_4\right)_2HPO_4,\right.$ Riedel-de Haen, Seelze, Germany), calcium nitrate tetrahydrate $\left(\mathrm{Ca\backslash:(NO_3)_2\cdot\ 4H_2O}\right)$, Merck, Darmstadt, Germany), sodium hydroxide (NaOH), cerium nitrate hexahydrate $\left(\left(\mathrm{Ce\backslash:(NO_3)_3}\right.\right.$.6$\mathrm{H_2O}$, Macklin, Shanghai, China), and sodium selenite pentahydrate (($\mathrm{Na_2\ SeO_3\cdot\ 5H_2O}$), Sigma-Aldrich, St. Louis, MO, USA). All chemicals were of analytical grade and used without further purification.

2.1. Synthesis of HA Nanoparticles

Nanohydroxyapatite (nHA) was synthesized hydrothermally. Briefly, calcium and phosphate precursor solutions were prepared by dissolving respective salts individually in distilled water, while maintaining a Ca/P ratio of 1.67. Then, the phosphate solution was added dropwise to the calcium solution under constant stirring, and the pH was maintained at 11. The resulting suspension was sonicated for 30 minutes and hydrothermally treated at 200°C for 8 hours with a heating rate of 5°C min^{-1}.

After cooling overnight, the precipitates were filtered, washed with deionized water, and dried at 70°C for 24 hours. The product was ground into a fine powder and calcined at 600°C for 90 minutes to improve crystallinity and remove adsorbed water (Figure S1), as decomposition of HA ß-tricalcium phosphate (ß-TCP) is reported at high calcination temperatures.[16, 17]

Table 1 summarized ion-substitution strategy used in the study. The required amounts of cerium and selenium were calculated as described in the supplementary data and incorporated into the respective calcium or phosphorus precursor solution. The synthesis was carried out using the same hydrothermal protocol as described for pure hydroxyapatite.

Table 1
Ion-substitution strategy used for the synthesis of hydroxyapatite; CS denotes Ce–Se co-substituted hydroxyapatite; CS-1 to CS-4 represent different experimental groups with varying Ce/Se molar ratios

Substitution Type	Sample ID	Cerium (mol%)	Selenium (mol%)
Non-substituted	HA	–	–
Monosubstituted	Ce-HA	2	–
	Se-HA	–	2
Co-substituted	CS-1	2	2
	CS-2	5	5
	CS-3	10	10
	CS-4	15	5

2.2. Characterizations

Fourier Transform Infrared Spectroscopy (FTIR) spectra were recorded using an FTIR spectrometer in the range of 4000 – 400 cm-1 with Attenuated Total Reflectance (ATR; 100 FT-IR, PerkinElmer, Shelton, CA, USA) at a resolution of 8 cm-1 and 64 scans. X-ray diffraction (XRD) analysis was performed using a diffractometer (Rigaku Ultima IV, Neu-Isenburg, Germany), over the 2θ range of 10–70°C at a scan rate of 2θ/min and a step size of 0.02, equipped with a Cu-Kα radiation source of 0.15406 nm. Phase identification was performed using the International Commission for Diffraction Data-Joint Committee on Powder Diffraction Standards (ICDD-JCPDS) database. The lattice parameters **a** and **c** were determined from the **(300)** reflection and using the **(002)** and **(004)** reflections, respectively. The crystallite size and lattice strain were calculated by the Debye-Scherrer formula and Williamson–Hall

method. Crystallinity was reported based on the sharpness of diffraction peaks and their full width at half maximum (FWHM) values. The detailed calculation procedure is mentioned in the Supplementary Document.

The elemental composition and oxidation states were determined using K-ALPHA radiation (Thermo Fisher Scientific, USA) with monochromatic Al K-alpha. Morphological analysis of nanoparticles was done using SEM (TESCAN VEGA 3, TESCAN, Brno, Czech Republic) at 10 KV after gold sputtering. The elemental composition was obtained using energy-dispersive X-ray spectroscopy (EDS) attached to the SEM. Specific surface area and pore characteristics were analyzed after degassing at 180°C for 12 hours under vacuum using Micromeritics ASAP 2020 Plus Analyser (USA). Zeta potential measurement was performed using a Zeta Sizer Nano series (Malvern Panalytical, UK) at 25°C.

2.3. Antimicrobial Activity

An agar well diffusion assay was used to assess the antimicrobial activity against *Staphylococcus aureus (S. aureus; ATCC 43300)*, *Escherichia coli (E. coli; ATCC 25922)*, *Klebsiella pneumoniae (K. pneumoniae; ATCC 1706)*, *Acinetobacter baumannii (A. baumannii; BAA-1710)*, and *Pseudomonas aeruginosa (P. aeruginosa; ATCC 27853).* Before testing, nanoparticle suspensions were prepared at 10 mg/mL in autoclaved distilled water and stored at 4°C for 24 hours.

Wells (6 mm) were loaded with 50 µL of nanoparticle suspension, and plates were stored at 4°C for 2 hours to allow diffusion. Tetracycline was used as a positive control. Antimicrobial activity was assessed by measuring inhibition zones after incubation at 37°C for 24 hours. The experiment was carried out in triplicate, and results were reported as mean ± S.D.

2.4. DPPH Free-Radical Scavenging Assay

The antioxidant potential of nanoparticles was evaluated using the 2,2-diphenyl-1-picrylhydrazyl (DPPH) assay [5]. Ascorbic acid served as a positive control. Nanoparticle suspensions (100, 200, 300, and 400 µg/mL) were prepared and mixed thoroughly with DPPH solution [18]. The reaction mixture was incubated at room temperature for 30 min in the dark, then centrifuged for 10 min at 6000 rpm [19]. The absorbance was measured at 517 nm using the Thermo Scientific Multiskan Sky spectrophotometer (Singapore). The DPPH radical-scavenging activity was calculated using the following formula:

$$\%\ DPPH\ Scavenging = \frac{Acontrol - Atest}{Acontrol} * 100 \quad \text{EQ.1}$$

where A control is the absorbance of the control (DPPH without the test sample), and A2 is the absorbance of test sample containing DPPH.

2.5. Anti-Inflammatory Assay

Anti-inflammatory activity was assessed using the bovine serum albumin (BSA) denaturation inhibition assay [18]. Samples at different concentrations (100, 200, 300, and 400 µg/mL) were added to 1% BSA. The mixture was incubated at 25°C for 10 min, then heated at 70°C for 20 min. The absorbance was

measured at 660 nm using the Thermo Scientific Multiskan Sky spectrophotometer (Singapore). Diclofenac sodium at a similar concentration was used as a positive control. The experiment was carried out in triplicate, and the percentage inhibition of protein denaturation was calculated using the given equation.

$$\%\ inhibition = \frac{A2-A1}{A2} * 100 \text{ EQ. 2}$$

where A1 is the absorbance of the sample, and A2 is the absorbance of the negative control

2.6. Cytocompatibility Testing

The MTT assay was performed on human gingival fibroblast-1 (HGF-1; CRL-2014) cells to evaluate cytocompatibility. Cells were cultured in Dulbecco's Modified Eagle Medium (DMEM), supplemented with 5% fetal bovine serum, 1% penicillin/streptomycin, and 2 mM L-glutamine at 37°C and 5% CO_2. Cells were seeded into 96-well plates at 5×10^3 cells/well and incubated for 24 hours to allow attachment. Culture media were then replaced with nanoparticle eluates (100, 10, and 1 µg/mL), and the plates were incubated for 48 hours.

MTT solution (200 µL) was added to each well and incubated for 4 hours, then dissolved in 100 µL DMSO. Untreated cells served as experimental control. Absorbance was measured at 540 nm using a MULTISKAN GO (Thermo Scientific, US), and cell viability was calculated as a percentage. Experiments were performed in triplicate. Results were expressed as mean ± standard deviation.

$$\text{Cell\:viability\:(\%)} = \frac{\text{Absorbance\:of\:treated\:cells}}{\text{Absorbance\:of\:control\:cells}} \times 100 \text{ EQ. 3}$$

2.7. Cytotoxicity assessment against CAL-27 Oral Squamous Carcinoma Cells

Cytotoxicity against Cal-27 human squamous cell carcinoma cells (CRL-2095) was evaluated under the same culture conditions as described for HGF-1 cells. Cells were seeded into a 96-well plate at a density of 30,000 cells/mL (100 µL/well) and incubated for 24 hours. Cells were then exposed to nanoparticle suspensions (100 µg/mL) for 24 hours. Cytotoxicity was evaluated using the MTT assay as described for HGF-1. Samples showing cytotoxic effect in initial screening were further evaluated at concentrations of 100, 75, 50, and 25 µg/mL. Cells were incubated for 24, 48, or 72 hours, and morphological changes following each treatment period were observed under an inverted microscope (10x).

2.8. Statistical Analysis

SPSS software (version 26; IBM Corp., USA) was used to analyze quantitative data. Data are presented as mean ± S.D. Normality was assessed using the Shapiro-Wilk test, and Levene's test evaluated homogeneity of variance. For normally distributed data, one-way analysis of variance (ANOVA) followed by Tukey's post hoc was used to compare nanoparticles. A p-value ≤ 0.05 was considered statistically significant.

3. Results

3.1. Composition and Structural Characterizations

FTIR analysis revealed that all samples retained the characteristic vibrational peaks of HA, including phosphate (PO43-) bands around 960 cm-1 (v1), 1020–1100 cm-1 (v3), and 560–603 cm-1 (v4), together with hydroxyl (OH^-) stretching bands at approximately 3570 cm-1 (Fig. 1a). Minor shifts in band intensity and position were observed in substituted samples. XRD further confirmed the preservation of the hexagonal apatite structure (Fig. 1b). The diffraction patterns of pure HA, indexed with JCPDS 09-0432, are presented in Figure S2. Diffraction peaks were observed at 2θ = 25.9˚ (002), 31.8˚ (211), 32.9˚ (300), 34.2˚ (202), 39.9˚ (310), 46.7˚ (222), 49.5˚ (213), 53.1˚ (004), and 64˚ (304).

Table 2 shows structural parameters calculated from XRD data. Ce-HA had reduced crystallite size and increased lattice strain, compared with HA. Similarly, Se substitution caused slight broadening and shifting of peaks, with a minor reduction in crystallite size and an increase in lattice strain. Co-substituted samples exhibited concentration-dependent structural changes in crystallite size and lattice strain.CS-1 and CS-2 exhibited a reduction in crystallite size compared with pure HA. In contrast, CS-3 had the smallest crystallite size and the highest lattice strain.

Table 2
Lattice parameters, unit cell volume and crystallite size of synthesized nanoparticles

Sample	Lattice Parameter (nm)		Unit cell Volume (nm^3)	Crystallite Size (nm)	Lattice Strain (10^{-3})
	a	c			
HA	0.9368	0.6843	0.5201	31.6	3.51
Ce-HA	0.9394	0.6870	0.5251	28	4.31
Se-HA	0.9404	0.6878	0.5268	31.1	3.85
CS-1	0.9373	0.6849	0.5211	27.4	4.43
CS-2	0.9384	0.6868	0.5238	23	4.96
CS-3	0.9431	0.6881	0.5300	18.3	7.12
CS-4	0.9400	0.6883	0.5267	30.2	4.86

XPS analysis was performed to determine the chemical state of the substituted ions (Fig. 2). Ca 2p spectra of synthesized nanoparticles exhibited symmetrical doublets in the range of 347.2 to 350 eV, while P 2p spectra exhibited doublet peaks at approximately 134eV and 134.6 eV, consistent with Ca^{2+} and P^{5+} in HA, respectively. The Ce 3d spectra for Ce-HA and the co-substituted sample contained features consistent with both Ce^{3+} and Ce^{4+} reference compounds (Fig. 2c), indicating a mixed Ce oxidation state. The Se 3d spectrum showed a peak at 58–60 eV, consistent with oxidized Se4 + state in

Se-HA and co-substituted samples (Fig. 2d). No additional features associated with cerium oxide, elemental selenium or metal selenides were observed.

EDS analysis confirmed that all samples were predominantly composed of calcium, phosphorus, and oxygen, while selenium and cerium were detected in substituted samples (Table 3). Ce-HA contained 0.3at% cerium, while Se-HA contained 1.38at% selenium. The co-substituted samples had increasing concentrations of Ce (0.49–3.27 at%) and Se (1.68–2.90 at%) across CS-1 to CS-4.

Table 3
Elemental Composition of synthesized nanoparticles obtained by EDS analysis

Sample ID	O (at%)	P(at%)	Ca(at%)	Se(at%)	Ce(at%)	Ca/P
HA	65.54	9.16	15.70	-	-	1.71
Ce-HA	67.11	11.66	18.19	-	0.30	1.56
Se-HA	63.93	12.84	18.40	1.38	-	1.43
CS-1	63.80	14.65	19.38	1.68	0.49	1.32
CS-2	61.40	14.45	21.03	1.93	1.19	1.46
CS-3	61.35	13.52	17.40	3.01	2.42	1.29
CS-4	56.72	16.62	19.18	2.90	3.27	1.15

3.2. Morphological and Surface Characterizations

SEM revealed that HA had dense, irregular, cauliflower-like agglomerates ranging from 5 to 30 μm (Fig. 3a). Ce-HA revealed smaller, loosely packed agglomerates with greater interparticle voids and increased surface roughness. Se-HA retained a morphology more similar to pure HA. Co-substituted samples showed a progressive increase in surface roughness, fragmentation, and interparticle porosity with increasing substitution level. CS-1 showed angular agglomerates with interconnected voids, while CS-3 had fragmented agglomerates with greater interparticle gaps. In contrast, CS-4 had more consolidated agglomerates with fewer interparticle gaps. Elemental mapping confirmed homogeneous distributions of Ce and Se in the co-substituted samples (Fig. 3b).

The observed changes in particle packing were further quantified through BET analysis (Table 4). All samples exhibited a type IV adsorption isotherm with H3 hysteresis. Pure HA had the lowest surface area, whereas co-substituted samples exhibited greater surface area ranging from 35.50 to 108.21 m^2/g. CS-4 exhibited the highest total pore volume.

The zeta potential ranged from − 14.5 to -27.8 mV, demonstrating composition-dependent differences in surface charge under the measurement conditions. CS-3 exhibited the least negative zeta potential, whereas CS-4 exhibited the most negative zeta potential (Table 4).

Table 4
BET parameters and Zeta potential of synthesized nanoparticles

Sample ID	Surface area (m^2/g)	Total pore volume (cm^3/g)	Average pore diameter (nm)	Zetapotential (mV)
HA	18.6116	0.169843	36.5026	-23.9
Ce-HA	19.1340	0.122246	25.5558	-21.7
Se-HA	20.1254	0.192696	20.1254	-23
CS-1	35.5000	0.381764	43.0156	-19
CS-2	64.3917	0.332898	20.6796	-18.3
CS-3	108.2092	0.429096	15.8617	-14.5
CS-4	98.1162	0.479847	19.5624	-27.8

3.3. Biological Evaluation

3.3.1. Antimicrobial Analysis

Antimicrobial activity of nanoparticles was influenced by the composition of nanoparticles and microbial species (Fig. 4). No measurable inhibition zones were observed against *E. coli* and *S. aureus*, while antimicrobial activity was observed against Klebsiella pneumoniae, Acinetobacter, and Pseudomonas aeruginosa. HA or Ce-HA had no measurable inhibition zone against any of the tested microbes. In contrast, inhibition zones of Se-HA were comparable to the positive control. The co-substituted samples exhibited intermediate activity, with CS-3 showing the largest inhibition zones.

3.3.2. Antioxidant and Anti-inflammatory Activities

Antioxidant activity showed dose-dependent inhibition of DPPH radicals (Fig. 5a). Pure HA exhibited significantly weaker radical-scavenging activity than the substituted HA. Co-substituted samples showed greater DPPH- scavenging activity than Ce-HA but activity comparable to Se-HA. Among the co-substituted samples, CS-2 and CS-4 exhibited the highest activity at the maximum tested concentration (Fig. 5b).

Anti-inflammatory activity, determined using the BSA denaturation assay, showed composition- and concentration-dependent effects (Fig. 5c). HA had significantly lower activity than substituted samples ($p < 0.001$), while Ce-HA had the highest activity. Pure HA showed only a modest increase at 400 µg/mL compared with 25 µg/mL ($p = 0.010$). In contrast, Ce-HA showed significant increases at 100 µg/mL ($p = 0.038$), 200 µg/mL ($p = 0.009$), and 400 µg/mL ($p = 0.007$), with activity plateauing between 200 and 400 µg/mL. Se-HA showed a similar trend, with significant improvement at 200 µg/mL ($p = 0.006$) and 400 µg/mL ($p = 0.001$) compared with 50 µg/mL, followed by a plateau. Co-substituted nanoparticles had

intermediate activity (Fig. 5d). CS-1 had the lowest activity, whereas CS-2 exhibited the highest activity, with a significant increase from 200 µg/mL onward ($p = 0.009$).

3.3.3. Cytocompatibility with HGF-1 cells

Cytocompatibility was evaluated using HGF-1 cells after 48 hours of incubation (Fig. 6a). Nanoparticle composition and concentration significantly affected cell viability ($F = 128.12$, $p \leq 0.001$) [15]. HA, Ce-HA, Se-HA, CS-1 and CS-2 maintained ≥70% cell viability across all tested concentrations. In contrast, CS-3 and CS-4 showed ≤70% cell viability at higher concentrations.

Tukey's post-hoc analysis indicated that at 25 µg/mL, pure HA, CS-3 and CS-4 had statistically similar cell viability, which was significantly lower than that of Ce-HA, Se-HA, CS-1, and CS-2 ($p \leq 0.001$). A similar trend was observed at 50 µg/mL, although CS-4 had reduced cell viability compared with pure HA. At 100 µg/mL, Ce-HA and Se-HA had statistically similar values, while CS-4 exhibited the lowest cell viability ($p < 0.001$).

3.3.4. Cytotoxicity against CAL-27 Oral Squamous Carcinoma Cells

The effect of nanoparticles on CAL-27 squamous cell carcinoma cells was evaluated using the MTT assay. Pure HA and mono-substituted HA had little effect on CAL-27 viability during initial screening (Fig. 6b). Among co-substituted samples, CS-4 produced the greatest reduction in cell viability, followed by CS-3, whereas CS-2 showed moderate cytotoxicity, and CS-1 showed no cytotoxic effect on CAL-27 cells.

Based on initial screening, CS-3 and CS-4 were evaluated further over 24, 48, and 72 hours at concentrations of 25–100µg/mL. A significant effect of concentration and treatment time on cell viability was observed ($p \leq 0.05$). At 24 hours, CS-4 had an IC_{50} value of 89.87 µg/ml, whereas CS-3 did not reach IC_{50}. At 48 hours, the IC_{50} values were 96.87 µg/ml and 83.48 µg/ml for CS-3 and CS-4, respectively. At 72 hours, the IC_{50} was 99.48 µg/mL for CS-3 and 76.39 /mL for CS-4.

Morphological observations supported the viability findings. Untreated CAL-27 cells maintained polygonal morphology and uniform cell distribution. CS-3 induced slight cellular rounding at 25–50 µg/ml after 24 hours, whereas at 75–100 µg/ml, increased cell shrinkage, cellular rounding, and reduced cell density were observed, which became more pronounced at 48 and 72 hours (Fig. 7). Similarly, CS-4 caused minimal changes at 25–50 µg/ml but induced marked cellular rounding, irregular cell morphology, partial loss of adherence, and reduced cell density at 50–100 µg/ml, particularly at 48 and 72 hours (Fig. 8).

4. Discussion

Cerium–selenium co-substituted hydroxyapatite nanoparticles were synthesized as a multifunctional biomaterial for potential use in infected oral bone defects, where simultaneously preventing infection, regulating oxidative stress, and suppressing inflammation are desirable. The findings indicate that co-substitution modifies physicochemical and morphological characteristics in a composition-dependent manner. Importantly, biological effects did not improve linearly with Ce/Se substitution level, suggesting that the physicochemical characteristics, rather than the total substituent concentration alone, influenced material performance.

4.1. Effect of co-substitution on Physicochemical Properties of HA

The retention of characteristic phosphate and hydroxyl vibrational bands in HA FTIR spectra indicated preservation of the apatite structure after co-substitution. Minor shifts in band intensity and position in substituted samples may reflect localized lattice distortion associated with Ce and Se incorporation [20]. A weak band observed around 890 cm^{-1} in Se-HA was consistent with previous reports of Se-substituted HA [21]. Progressive peak broadening in co-substituted materials with increasing Ce-Se substitution further suggested increasing structural modification.

XRD analysis further supported preservation of hexagonal apatite structure after substitution. Ce-HA exhibited reduced crystallite size and increased lattice strain, compared with HA. These changes may reflect limited crystalline growth caused by differences between ionic radii and charge state of Ce^{+3}/Ce^{+4} and Ca^{+2} ions [20]. Ciobanu et al. observed similar changes in the XRD peaks of the Ce-doped hydroxyapatite/collagen layer [2].

Selenium incorporation produced comparatively subtle changes in the diffraction pattern, accompanied by a minor reduction in crystallite size and increased lattice strain, likely due to the differences in structural orientation and charge distribution of SeO_3^{2-} and PO_4^{3-} ions [23]. Structural modification upon Se incorporation is consistent with previous studies, although the magnitude of these changes depends on the extent of substitution and synthesis conditions [21, 22].

Co-substituted samples exhibited more pronounced concentration-dependent structural changes, in agreement with previous studies[24, 25]. From CS-1 to CS-3, crystallite size decreases and lattice strain increases compared with pure HA, suggesting increasing Ce and Se content led to more pronounced structural distortion. CS-4, however, deviated from this trend, indicating structural modification was not solely governed by total substitution level, but the Ce-to-Se ratio may also influence crystal growth.

XPS analysis provided additional information on the chemical state of incorporated elements. Features consistent with both Ce^{3+} and Ce^{4+} indicated a mixed Ce oxidation state in Ce-containing samples. The ability of cerium to exist in reversible Ce^{3+}/Ce^{4+} oxidation states are responsible for the redox behaviour of cerium-based nanomaterials and may therefore contribute to the antioxidant activity of Ce-based HA samples [26]. The Se 3d spectrum was consistent with the oxidized Se^{4+} state in Se-containing samples.

The absence of distinct XPS features associated with cerium oxide, elemental selenium, and metal selenides was consistent with previous reports.[21, 27]

EDS analysis confirmed that all samples were predominantly composed of calcium, phosphorus, and oxygen, with selenium and cerium additionally detected in the respective substituted samples. The measured concentrations of the substituent ions were lower than the amount added during synthesis, as has also been observed in substituted HA systems [9, 14, 21]. Nevertheless, the progressive increase in measured Ce and Se concentration from CS1- to CS-4 confirmed composition-dependent enrichment of the co-substituted samples.

Ce-HA showed a reduction in particle size, an effect that has been reported previously [20]. In contrast, selenium incorporation produced limited changes in particle packing [21]. In co-substituted samples, increased fragmentation was observed across CS-1 to CS-3, while CS-4 had more consolidated agglomerates. These morphological changes complemented the XRD observations, further suggesting that the physicochemical characteristics of the co-substituted materials were influenced by relative Ce/Se composition rather than total substitution level.

Changes in surface area and pore characteristics accompanied the observed morphological variations. Co-substituted samples had enhanced surface area and pore volume than HA, with CS-3 exhibiting the greatest surface area. Increased surface area and porosity may facilitate interaction of nanoparticles with their surrounding biological environment and potentially influence biological activity [25]. Composition-dependent differences were also observed in the zeta potential. A progressively less negative zeta potential from CS-1 to CS-3 indicated reduced electrostatic stability and a greater tendency towards agglomeration [2].

4.2. Effect of co-substitution on Biological Properties of HA

The antimicrobial response was both composition-dependent and microbe-specific, consistent with literature on ion-substituted calcium phosphate materials [28]. Inhibition of *Klebsiella pneumoniae*, *Acinetobacter*, and *Pseudomonas aeruginosa* are clinically relevant pathogens, given their association with oral and bone infections. Pure HA and Ce-HA produced no inhibition zones, which agrees with reported limited intrinsic antimicrobial activity of these nanoparticles [2, 29, 30]. In contrast, Se-HA had greater antimicrobial activity, with inhibition zones comparable to positive control. Previous studies have associated selenium-induced oxidative stress, disruption of microbial membranes, and inhibition of cellular enzymes responsible for these findings [29, 31]. Among co-substituted samples, CS-3 exhibited the largest inhibition zones. This may be due to relatively high selenium content, reduced crystallite size and greatest surface area. These characteristics may increase ion release, potentially influencing antimicrobial properties [28, 31].

Composition- and concentration-dependent differences were also evident in antioxidant and anti-inflammatory assays [18]. Pure HA exhibited significantly weaker radical-scavenging activity and anti-

inflammatory activity compared to the substituted HA, indicating that ionic substitution was primarily responsible for the enhanced biological responses [19, 32]. The antioxidant activity of co-substituted samples was higher than Ce-HA and comparable to Se-HA. CS-2 and CS-4 exhibited the highest antioxidant activity among the co-substituted samples. The improved antioxidant activity of CS-4 may be related to higher cerium content and coexistence of Ce^{3+} and Ce^{4+} as identified by XPS. A reversible Ce^{3+}/Ce^{4+} transition is associated with the ROS-scavenging properties of cerium-based nanomaterials[33].

The anti-inflammatory assay showed a different composition-dependent response. Ce-HA had the highest anti-inflammatory activity, consistent with literature that linked anti-inflammatory effects of cerium-containing nanomaterials to Ce^{3+}/Ce^{4+} redox cycling and suppression of pro-inflammatory cytokines [34, 35]. Among co-substituted nanoparticles, CS-1 exhibited the lowest anti-inflammatory activity, whereas CS-2 exhibited the highest activity. Despite their greater substituent concentration, CS-3 and CS-4 showed comparatively lower activity than CS-2, suggesting increasing substitution alone does not enhance anti-inflammatory response. Notably, CS-2 combined moderate structural modifications with enhanced surface area, which may have contributed to its greater activity.

Cytocompatibility with HGF-1 cells was also dependent on nanoparticle composition and concentration [15]. HA, Ce-HA, Se-HA, CS-1 and CS-2 met ISO 10993-5 criteria for non-cytotoxicity, whereas higher-substituted CS-3 and CS-4 showed reduced cytocompatibility at higher concentrations.

CS-1 and CS-2 showed significantly higher cell viability across concentrations, suggesting moderate substitution can preserve/ enhance cytocompatibility, potentially reflecting a balance between ionic composition and surface characteristics[15, 25]. In contrast, reduced viability associated with CS-3 and CS-4 indicates that higher substituent concentration may lead to greater cellular exposure to incorporated ions and burst ion release [32].

A contrasting composition-dependent response was observed in CAL-27 oral squamous cell carcinoma cells. Squamous cell carcinoma (SCC) is considered one of the most prevalent and malignant tumors of the head and neck region [13]. Pure HA and mono-substituted HA had little effect on CAL-27 viability, whereas CS-3 and CS-4 produced greater concentration- and time-dependent reduction in cell viability.

The enhanced cytotoxicity of highly substituted formulations suggests that the combined Ce-Se composition influences their interaction with carcinoma cells. The greater lattice distortion due to increased substituent concentration may promote higher ion release, causing impaired mitochondrial function and cellular stress [32]. Moreover, selenium can exert anticancer effects through increased intracellular ROS in malignant cells [36]. Wen et al. also reported that selenite induced apoptosis in CAL-27 cells [13].

Interestingly, the different responses of HGF-1 and CAL-27 are particularly noteworthy. CS-3 and CS-4 showed reduced CAL-27 viability while maintaining relatively high HGF-1 viability, suggesting preferential

cytotoxicity towards carcinoma cells. This response was most pronounced for CS-4 and coincides with its higher substituent content and distinct physicochemical characteristics.

Collectively, the findings demonstrate that the biological performance of Ce-Se-substituted HA depends not only on substituent concentration but also on the physicochemical characteristics of the material. However, further studies are required to investigate ion uptake and release, intracellular ROS generation, optimize substituent concentration and establish a comprehensive biosafety profile.

5. Conclusions

Cerium-selenium co-substituted HA nanoparticles were successfully synthesized as multifunctional biomaterials, with their physicochemical and biological properties strongly influenced by the degree of substitution. Moderate substitution (CS-2) had favourable HGF-1 cytocompatibility and anti-inflammatory and antioxidant activity, and antibacterial activity. At higher substitution levels (CS-3 and CS-4), greater cytotoxicity against CAL-27 cells was observed while maintaining high viability of HGF-1, indicating differential response between the normal and malignant oral cells. These findings demonstrate the potential of Ce-Se co-substitute HA towards different biological functions

Declarations

Credit authorship contribution statement

Asfia Saeed: Conceptualization, Methodology, Investigation, Formal Analysis and Writing-original draft

Aalia Khanem: Methodology, Investigation, Validation

Farwa Naqvi: Methodology, Investigation, Validation

Maria Khalid: Investigation, Validation

Farhan Younas: Resources, Supervision, Methodology, Validation, Writing- review and editing

Almas Jabeen: Resources, Supervision, Methodology, Validation

Muhammad Nawaz: Investigation, Formal Analysis, Validation

Talha Nisar: Investigation, Formal Analysis, Validation

Veit Wagner: Investigation, Formal Analysis, Validation

Muhammad Raza Shah: Resources, Supervision

Ali Haider: Conceptualization, Resources, Supervision, Validation, Writing- review and editing

Abdul Samad Khan: Conceptualization, Resources, Supervision, Writing- review and editing

Acknowledgements

The authors acknowledge Prof. Anwar Ali Shah, Dr. Muhammad Khan Asif, and Dr. Saba Omer from Shifa College of Dentistry, Islamabad, for facilitating this study.

Funding

This research received no specific grant from funding agencies in the public, commercial, or non-profit sectors.

Declaration of competing interests

The authors declare no competing financial interests.

Data Availability Statement

The data supporting the findings of this study are available in the article and its supplementary information and are also available on request.

Declaration of generative AI use

The authors used ChatGPT in preparing the graphical abstract. After using this tool, the authors reviewed the content and took full responsibility for the published article.

References

1. Habib MdL, Disha SA, Sahadat Hossain Md, Uddin MdN, Ahmed S. Enhancement of antimicrobial properties by metals doping in nano-crystalline hydroxyapatite for efficient biomedical applications. Heliyon 2024;10:e23845. https://doi.org/10.1016/j.heliyon.2023.e23845.
2. Ciobanu G, Harja M. Cerium-doped hydroxyapatite/collagen coatings on titanium for bone implants. Ceram Int 2019;45:2852–7. https://doi.org/10.1016/j.ceramint.2018.07.290.
3. Gayathri B, Muthukumarasamy N, Velauthapillai D, Santhosh SB, asokan V. Magnesium incorporated hydroxyapatite nanoparticles: Preparation, characterization, antibacterial and larvicidal activity. Arab J Chem 2018;11:645–54. https://doi.org/10.1016/j.arabjc.2016.05.010.
4. He W, Xu T, Wang M, Ni N, Su Y, Fan X. ROS-scavenging nanomaterials as emerging tools for bone tissue regeneration: A comprehensive review of recent progress. Acta Pharm Sin B 2025;15:6274–306. https://doi.org/10.1016/j.apsb.2025.09.040.
5. Murugesan V, Kreedapathy GE, Vaiyapuri M. Evaluation of the Antioxidant, Antimicrobial, Haemolytic and Cytotoxic Effect of Eggshell Based Hydroxyapatite. J Clust Sci 2022;33:825–34. https://doi.org/10.1007/s10876-021-02153-x.
6. Kubiak-Mihkelsoo Z, Kostrzębska A, Błaszczyszyn A, Pitułaj A, Dominiak M, Gedrange T, et al. Ionic Doping of Hydroxyapatite for Bone Regeneration: Advances in Structure and Properties over Two

Decades—A Narrative Review. Appl Sci 2025;15:1108. https://doi.org/10.3390/app15031108.

7. Graziani G, Boi M, Bianchi M. A Review on Ionic Substitutions in Hydroxyapatite Thin Films: Towards Complete Biomimetism. Coatings 2018;8:269. https://doi.org/10.3390/coatings8080269.
8. Wang D, Guo M, Gao Y, Gao S, Yin W, Song W. Synthesis and evaluation of resveratrol–cerium modified hydroxyapatite for enhanced bone repair scaffolds. RSC Adv 2026;16:10565–81. https://doi.org/10.1039/D5RA10060G.
9. Singh S, Jain RK. The Synthesis, Characterization, and Assessment of Antibacterial Properties of an Orthodontic Adhesive Containing Cerium-Substituted Hydroxyapatite Nanoparticles: An In Vitro Study. Cureus 2024. https://doi.org/10.7759/cureus.52177.
10. Pandey A, Midha S, Sharma RK, Maurya R, Nigam VK, Ghosh S, et al. Antioxidant and antibacterial hydroxyapatite-based biocomposite for orthopedic applications. Mater Sci Eng Biol Appl 2018;88:13–24. https://doi.org/10.1016/j.msec.2018.02.014.
11. Tsamesidis I, Gkiliopoulos D, Pouroutzidou GK, Lymperaki E, Papoulia C, Reybier K, et al. Effect of Artemisinin-Loaded Mesoporous Cerium-Doped Calcium Silicate Nanopowder on Cell Proliferation of Human Periodontal Ligament Fibroblasts. Nanomaterials 2021;11:2189. https://doi.org/10.3390/nano11092189.
12. Zastulka A, Clichici S, Tomoaia-Cotisel M, Mocanu A, Roman C, Olteanu C-D, et al. Recent Trends in Hydroxyapatite Supplementation for Osteoregenerative Purposes. Materials 2023;16:1303. https://doi.org/10.3390/ma16031303.
13. Wen X, Zhou Q, Lin S, Mai H, Zhang L. Selenium-modified hydroxyapatite titanium coating: enhancing osteogenesis and inhibiting cancer in bone invasion by head and neck squamous cell carcinoma. Front Bioeng Biotechnol 2025;13. https://doi.org/10.3389/fbioe.2025.1552661.
14. Wang Y, Ma J, Zhou L, Chen J, Liu Y, Qiu Z, et al. Dual functional selenium-substituted hydroxyapatite. Interface Focus 2012;2:378–86. https://doi.org/10.1098/rsfs.2012.0002.
15. Ressler A, Žužić A, Ivanišević I, Kamboj N, Ivanković H. Ionic substituted hydroxyapatite for bone regeneration applications: A review. Open Ceramics 2021;6:100122. https://doi.org/10.1016/j.oceram.2021.100122.
16. Sahadat Hossain Md, Ahmed S. FTIR spectrum analysis to predict the crystalline and amorphous phases of hydroxyapatite: a comparison of vibrational motion to reflection. RSC Adv 2023;13:14625–30. https://doi.org/10.1039/D3RA02580B.
17. Fathi MH, Hanifi A, Mortazavi V. Preparation and bioactivity evaluation of bone-like hydroxyapatite nanopowder. J Mater Process Technol 2008;202:536–42. https://doi.org/10.1016/j.jmatprotec.2007.10.004.
18. Ragini B, Kandhasamy S, Jacob JP, Vijayakumar S. Synthesis and in vitro characteristics of biogenic-derived hydroxyapatite for bone remodeling applications. Bioprocess Biosyst Eng 2024;47:23–37. https://doi.org/10.1007/s00449-023-02940-y.
19. Kumar R, Shikha D, Sinha SK. DPPH radical scavenging assay: A tool for evaluating antioxidant activity in 3% cobalt – Doped hydroxyapatite for orthopaedic implants. Ceram Int 2024;50:13967–

73. https://doi.org/10.1016/j.ceramint.2024.01.314.
20. Moaness M, Mousa SM, Abo-Elfadl MT, El-Bassyouni GT. Doxorubicin loaded cerium substituted hydroxyapatite nanoparticles: A promising new therapeutic approach for bone regeneration, doxorubicin delivery, and cancer treatment. Int J Pharm 2024;654:123969. https://doi.org/10.1016/j.ijpharm.2024.123969.
21. Alkan B, Durucan C. Complete chemical and structural characterization of selenium-incorporated hydroxyapatite. J Mater Sci Mater Med 2022;33:5. https://doi.org/10.1007/s10856-021-06631-6.
22. Pajor K, Pajchel L, Kolodziejska B, Kolmas J. Selenium-Doped Hydroxyapatite Nanocrystals–Synthesis, Physicochemical Properties and Biological Significance. Crystals (Basel) 2018;8:188. https://doi.org/10.3390/cryst8050188.
23. Gao J, Huang J, Shi R, Wei J, Lei X, Dou Y, et al. Loading and Releasing Behavior of Selenium and Doxorubicin Hydrochloride in Hydroxyapatite with Different Morphologies. ACS Omega 2021;6:8365–75. https://doi.org/10.1021/acsomega.1c00092.
24. Shepherd JH, Shepherd D V., Best SM. Substituted hydroxyapatites for bone repair. J Mater Sci Mater Med 2012;23:2335–47. https://doi.org/10.1007/s10856-012-4598-2.
25. Paramasivan M, Sampath Kumar TS, Kanniyappan H, Muthuvijayan V, Chandra TS. Biomimetic ion substituted and Co-substituted hydroxyapatite nanoparticle synthesis using Serratia Marcescens. Sci Rep 2023;13:4513. https://doi.org/10.1038/s41598-023-30996-z.
26. Vinicius Beserra dos Santos M, Bastos Nogueira Rocha L, Gomes Vieira E, Leite Oliveira A, Oliveira Lobo A, de Carvalho MAM, et al. Development of Composite Scaffolds Based on Cerium Doped-Hydroxyapatite and Natural Gums—Biological and Mechanical Properties. Materials 2019;12:2389. https://doi.org/10.3390/ma12152389.
27. He L, Li H, Chen X, Xu T, Sun T, Huang H, et al. Selenium-substituted hydroxyapatite particles with regulated microstructures for osteogenic differentiation and anti-tumor effects. Ceram Int 2019;45:13787–98. https://doi.org/10.1016/j.ceramint.2019.04.075.
28. Hassanain M, Abdel-Ghafar HM, Hamouda HI, El-Hosiny FI, Ewais EMM. Enhanced antimicrobial efficacy of hydroxyapatite-based composites for healthcare applications. Sci Rep 2024;14:26426. https://doi.org/10.1038/s41598-024-76088-4.
29. Kamphof R, Lima RNO, Schoones JW, Arts JJ, Nelissen RGHH, Cama G, et al. Antimicrobial activity of ion-substituted calcium phosphates: A systematic review. Heliyon 2023;9:e16568. https://doi.org/10.1016/j.heliyon.2023.e16568.
30. Lin Y, Yang Z, Cheng J. Preparation, Characterization and Antibacterial Property of Cerium Substituted Hydroxyapatite Nanoparticles. J Rare Earths 2007;25:452–6. https://doi.org/10.1016/S1002-0721(07)60455-4.
31. Muthusamy S, Mahendiran B, Sampath S, Jaisankar SN, Anandasadagopan SK, Krishnakumar GS. Hydroxyapatite nanophases augmented with selenium and manganese ions for bone regeneration: Physiochemical, microstructural and biological characterization. Materials Science and Engineering: C 2021;126:112149. https://doi.org/10.1016/j.msec.2021.112149.

32. Barbanente A, Di Cosola AM, Rizzi F, Depalo N, Comparelli R, Castaldo R, et al. Development of dual acting selenium-doped hydroxyapatite nanoparticles with platinum-bisphosphonate complexes for bone cancer therapy. RSC Adv 2026;16:10100–12. https://doi.org/10.1039/D5RA09348A.
33. Celardo I, Pedersen JZ, Traversa E, Ghibelli L. Pharmacological potential of cerium oxide nanoparticles. Nanoscale 2011;3:1411. https://doi.org/10.1039/c0nr00875c.
34. Corsi F, Deidda Tarquini G, Urbani M, Bejarano I, Traversa E, Ghibelli L. The Impressive Anti-Inflammatory Activity of Cerium Oxide Nanoparticles: More than Redox? Nanomaterials 2023;13:2803. https://doi.org/10.3390/nano13202803.
35. Duan Y, Zheng K, Hu W, Chen JJ, Lu X, Wang M, et al. Anti-inflammatory cerium-containing nano-scaled mesoporous bioactive glass for promoting regenerative capability of dental pulp cells. Int Endod J 2024;57:727–44. https://doi.org/10.1111/iej.14055.
36. Radomska D, Czarnomysy R, Radomski D, Bielawski K. Selenium Compounds as Novel Potential Anticancer Agents. Int J Mol Sci 2021;22:1009. https://doi.org/10.3390/ijms22031009.

Figures

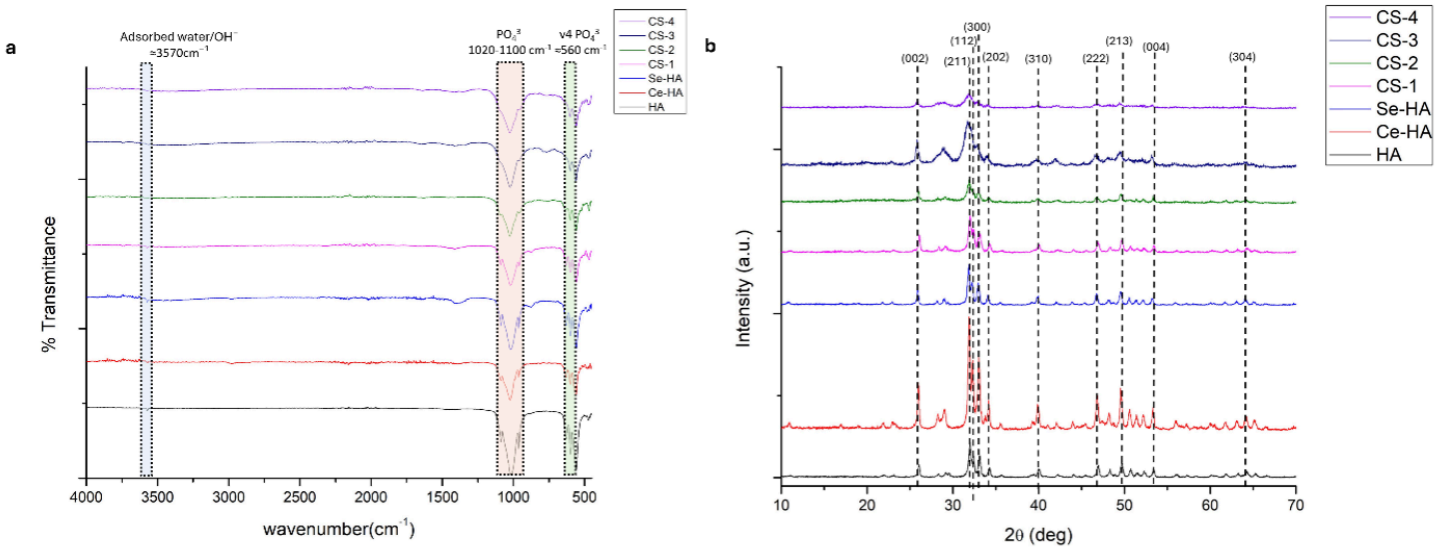


Figure 1

(a) FTIR spectra of synthesized nanoparticles recorded over the range of 4000-400cm^{-1}, showing characteristic phosphate (PO_4^{3-}) and hydroxyl (OH^-) absorption bands; (b) XRD pattern of synthesized nanoparticles showing characteristic peaks of the hydroxyapatite phase, matching JCPDS card no. 09-0432

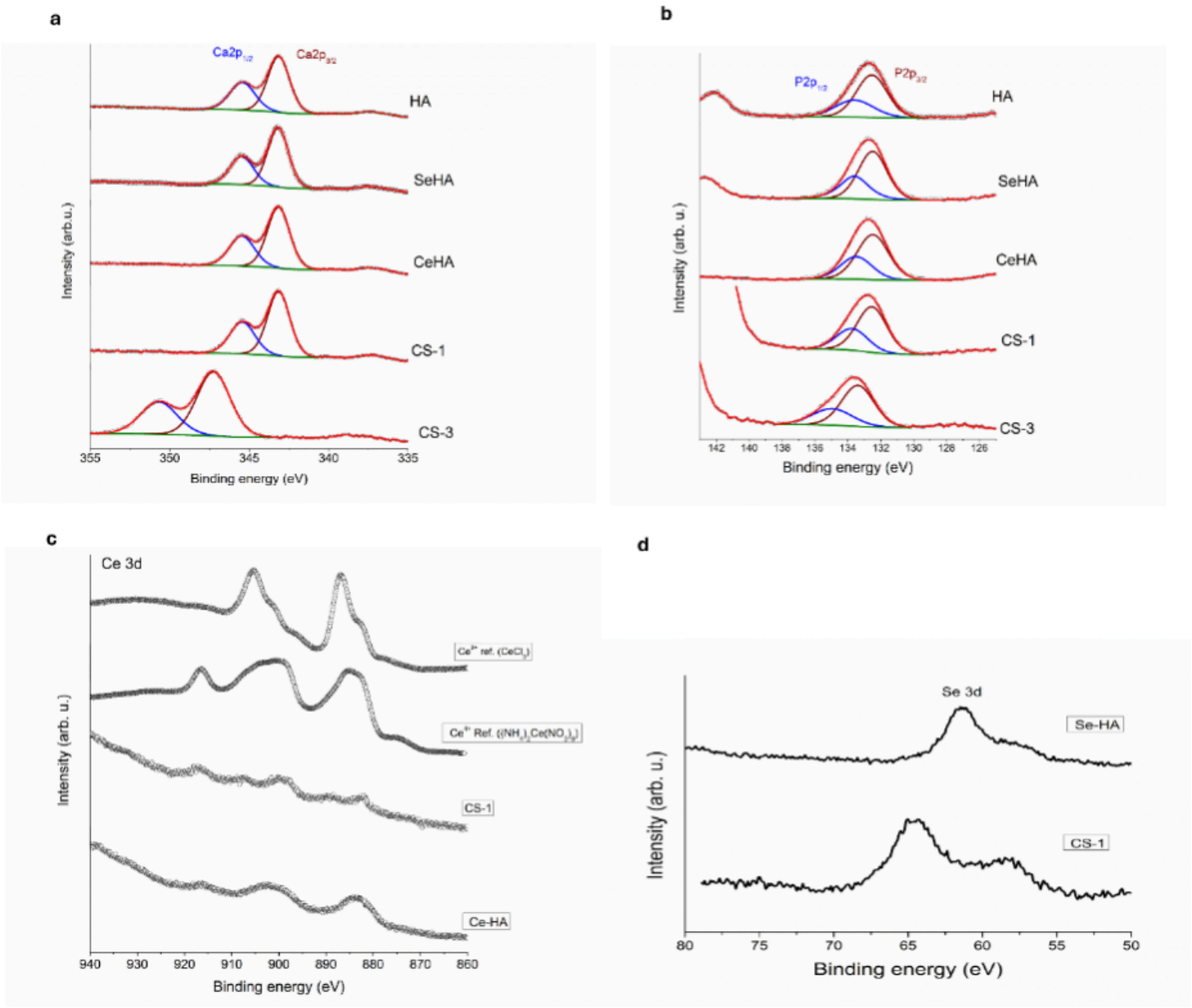


Figure 2

XPS analysis of HA and ion- substituted nanoparticles. (a) Ca 2p spectra of HA, Ce-HA, Se-HA, CS-1 and Cs-3 showing the characteristic spin-orbit doublets (b) P 2p showing the characteristic P $2p_3/_2$ and P $2p_1/_2$ spin-orbit doublets (c) High-resolution Ce 3d region of Ce-HA and CS-1, together with Ce^{3+} and Ce^{4+} reference spectra (d) High resolution Se 3d region of Se-HA and CS-1

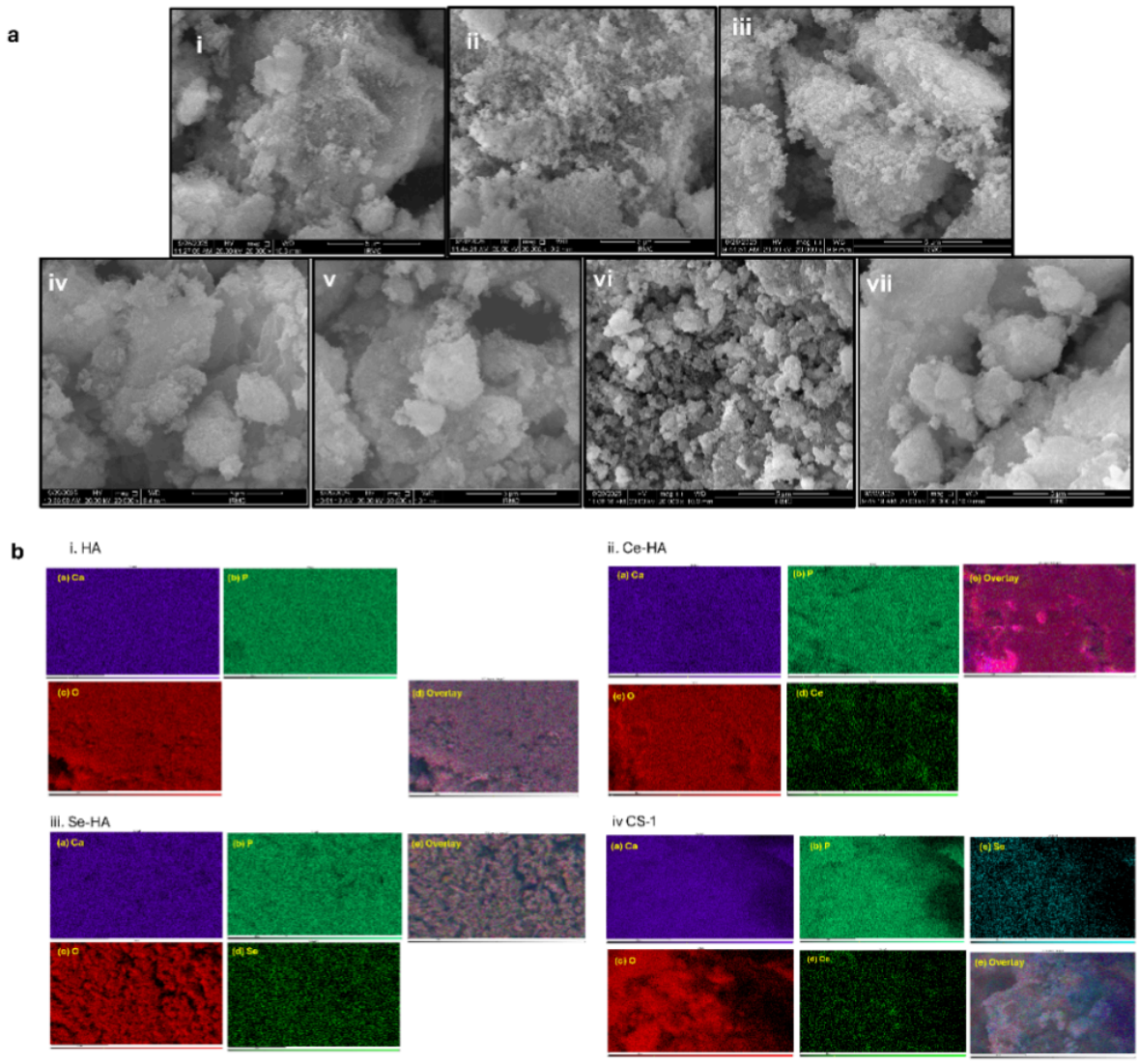


Figure 3

(a) SEM micrograph of synthesized nanoparticles at 20000X (scale bar 5μm) (i) HA, (ii) Ce-HA, (iii) Se-HA, (iv) CS-1, (v) CS-2, (vi) CS-3 and (vii) CS-4, (b) Elemental mapping of (i) HA, (ii) Ce-HA, (iii) Se-HA and (iv) Ce-Se co-substituted HA, showing the distribution of Ca, P, Ce, and Se.

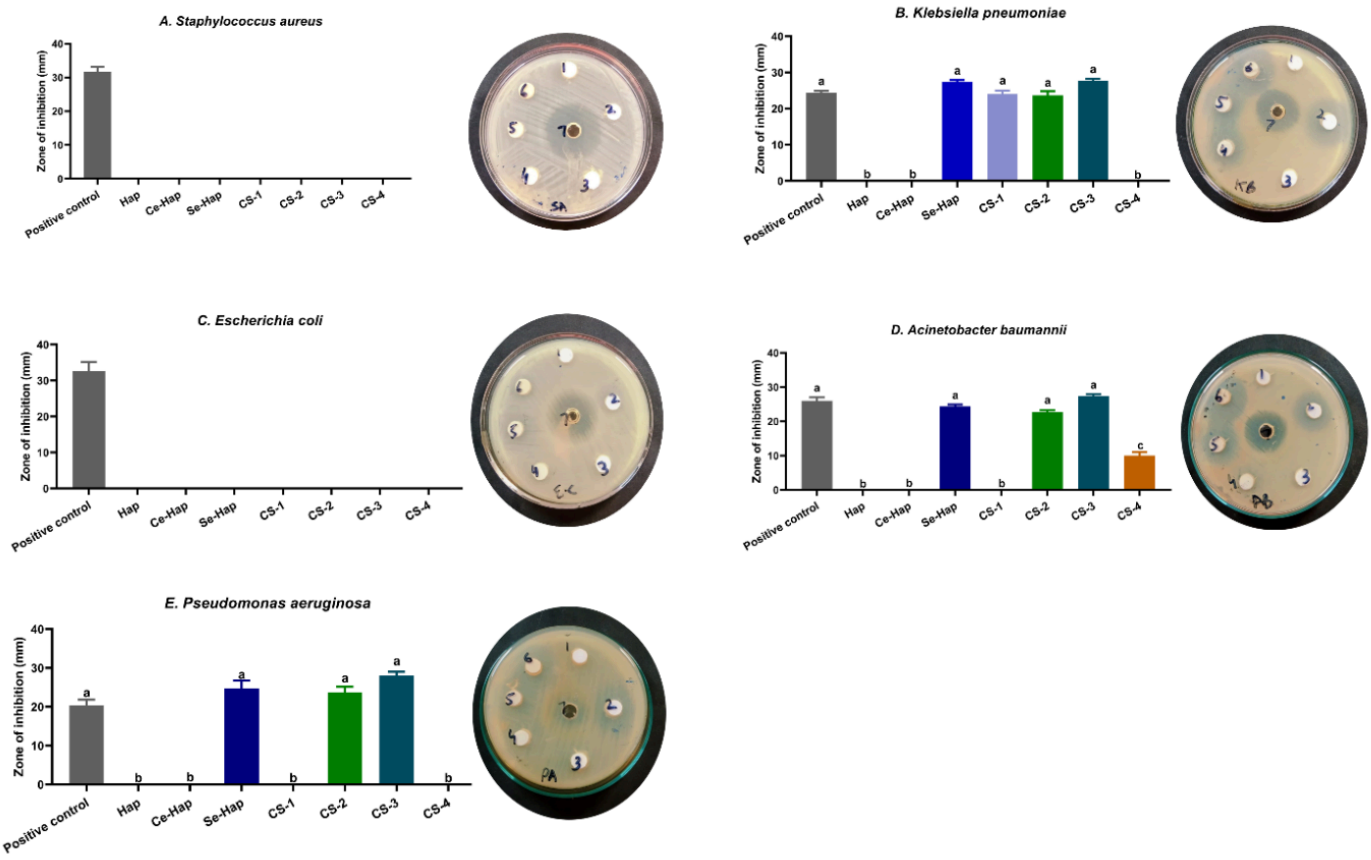


Figure 4

Mean zone of inhibition (n=3) of synthesized nanoparticles (a) *Acinetobacter baumannii*, (b) *Pseudomonas aeruginosa*, (c) *Klebsiella pneumoniae,*(d) *Escherichia coli*, and (e) *Staphylococcus aureus*; 1, HA; 2, Se-HA; 3, Ce-HA; 4, CS-1; 5, CS-2; 6, CS-3; and 7, positive control (tetracycline)

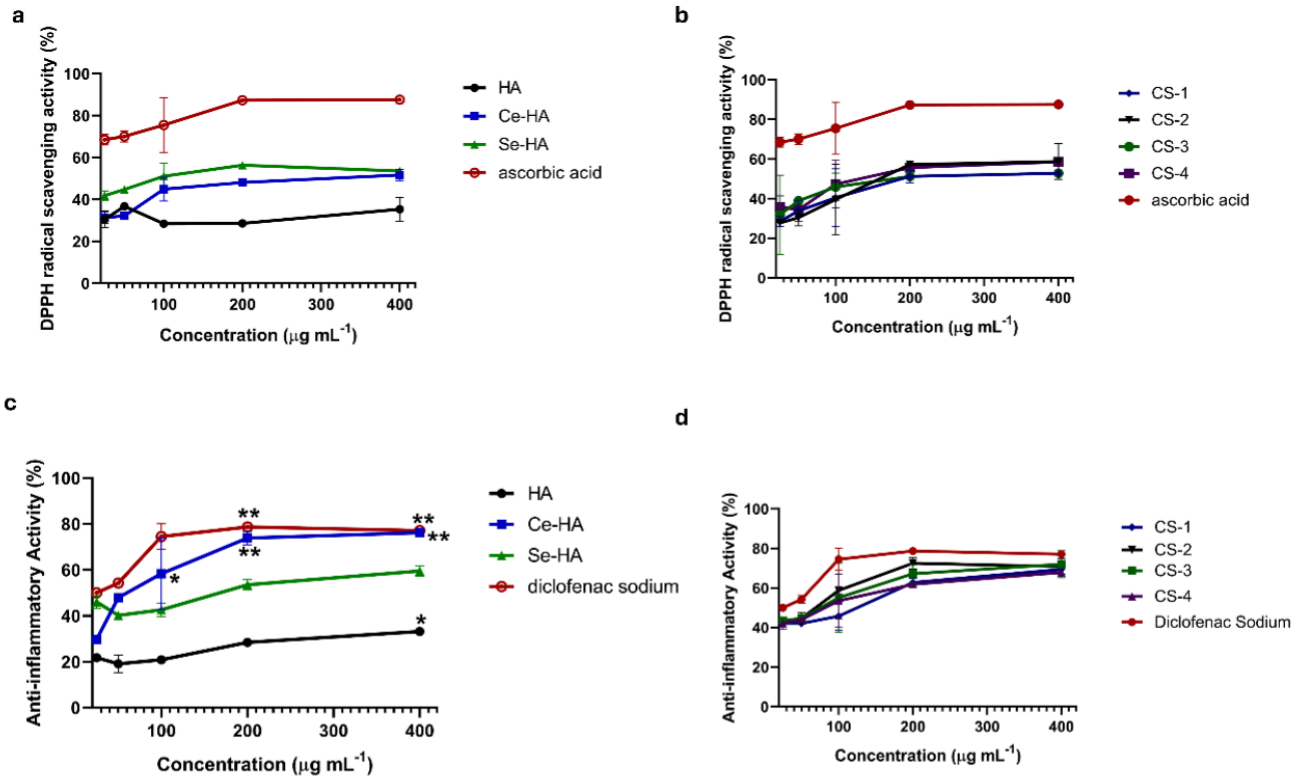


Figure 5

Antioxidant and anti-inflammatory activities of synthesized nanoparticles at 25, 50, 100, 200 and 400 µg/mL (a) DPPH radical scavenging activity of HA, Ce-HA and Se-HA, compared with positive control (ascorbic acid) (b) DPPH radical scavenging activity of co-substituted samples; (c) Anti-inflammatory activity of HA, Ce-HA, Se-HA with diclofenac sodium as positive control; (d) anti-inflammatory activity of co-substituted samples. Data are presented as mean ± S.D (n=3); *p≤0.05 was considered statistically significant.

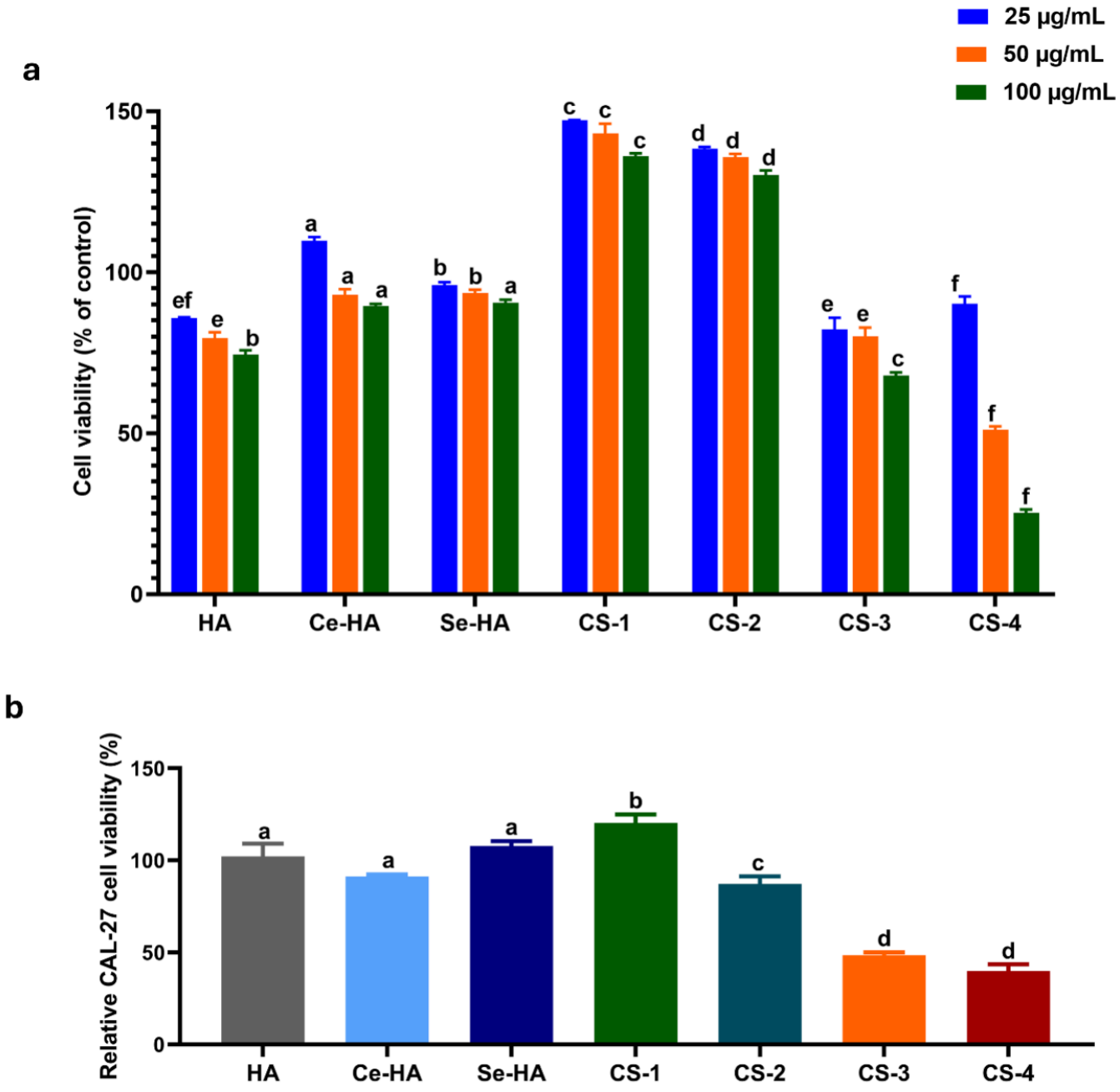


Figure 6

(a) Cell viability of HGF-1 cells (CRL-2014) after 48 h exposure to nanoparticles at 25, 50, and 100 µg/mL (b) Cell viability of CAL-27 cells (CRL-2095) after treatment with nanoparticles at 100 µg/mL. Data is presented as mean ± S.D (n=3). Different letters indicate statistically significant differences among samples ($p \leq 0.05$).

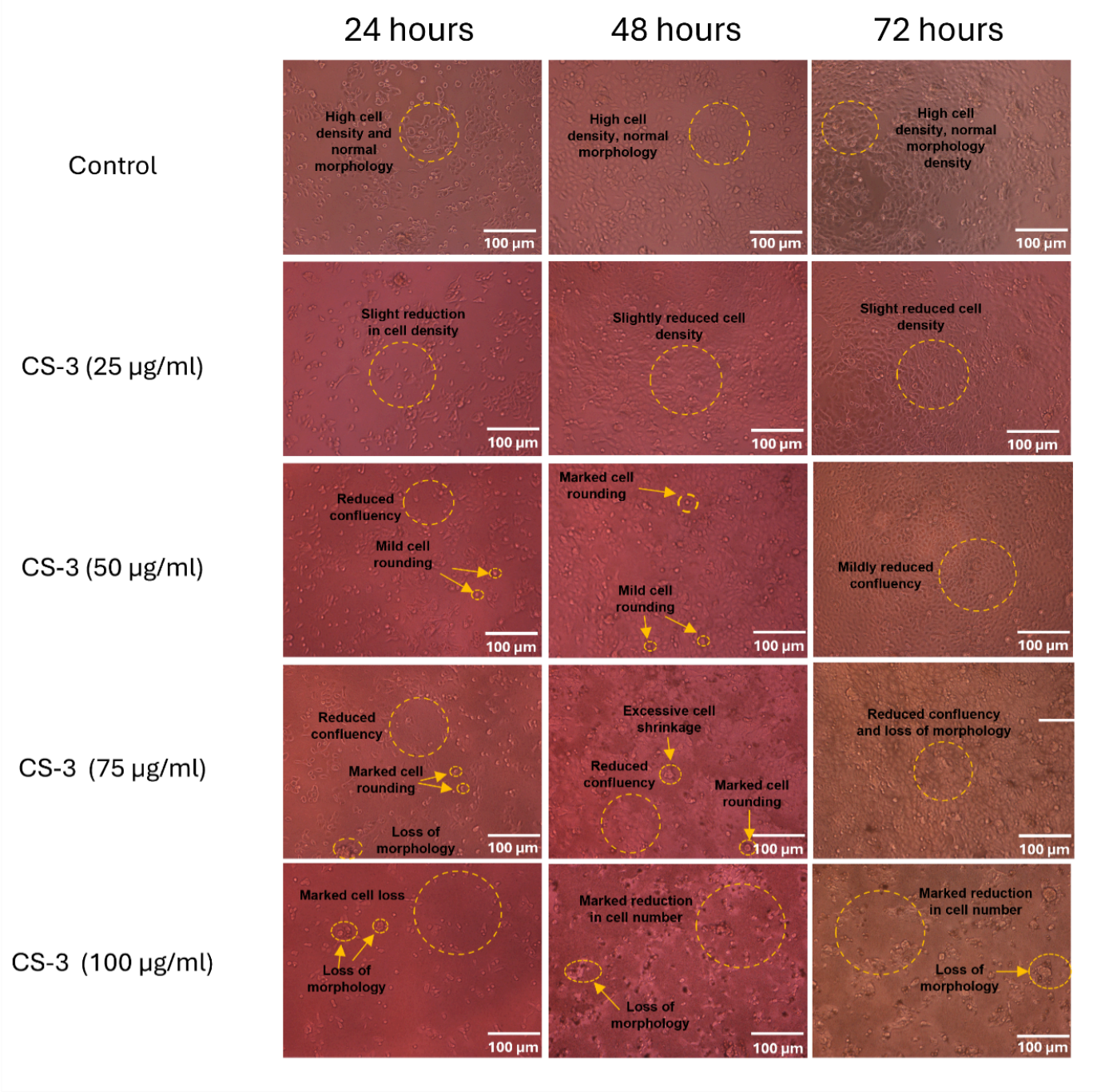


Figure 7

Phase-contrast images showing morphological changes in CAL-27 cells after treatment with CS-3 nanoparticles at concentrations of 25–100 µg/mL for 24, 48 and 72 hours

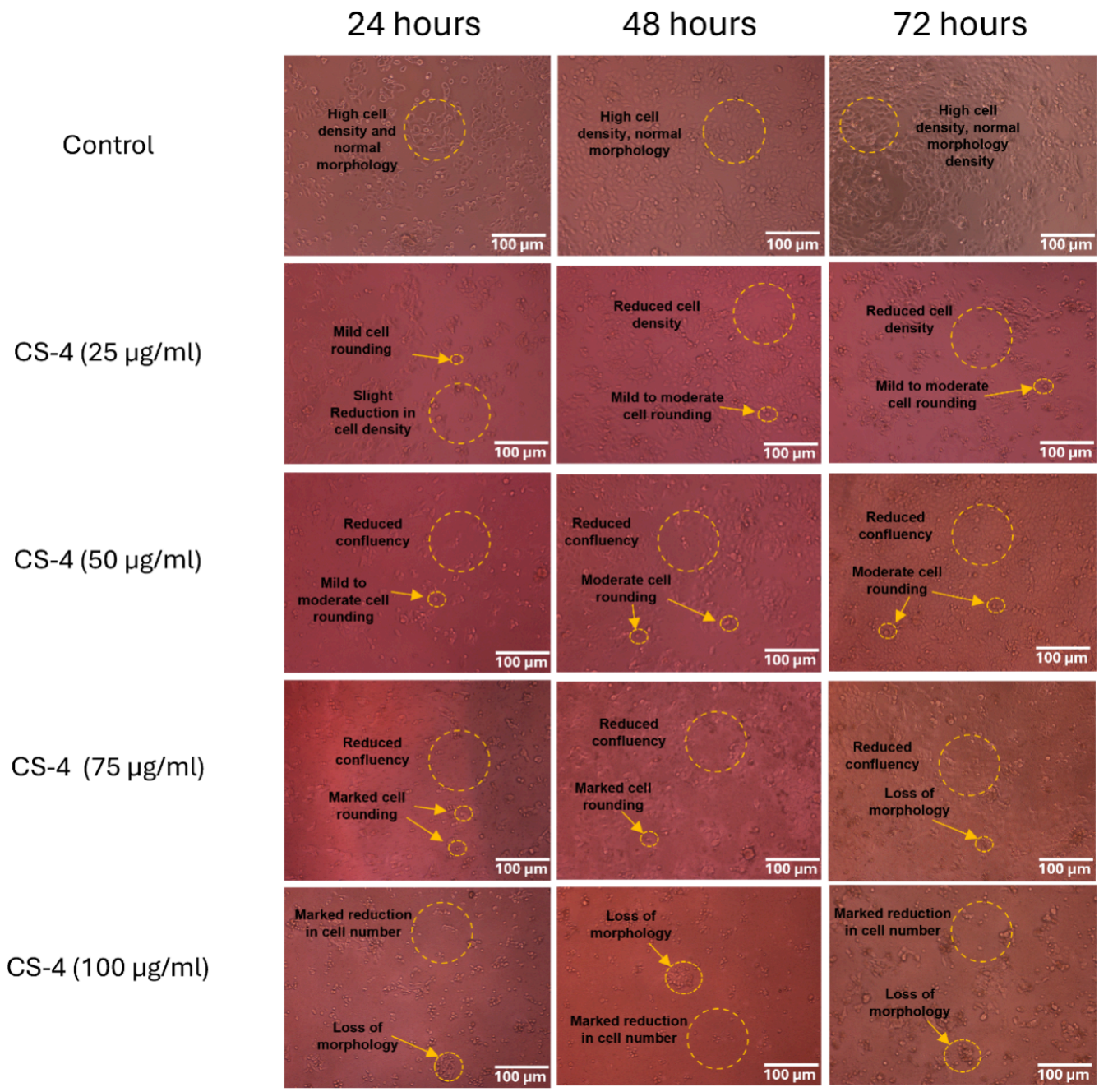


Figure 8

Phase-contrast images showing morphological changes in CAL-27 cells after treatment with CS-4 nanoparticles at concentrations of 25–100 µg/mL for 24, 48 and 72 hours.

Supplementary Files

This is a list of supplementary files associated with this preprint. Click to download.

- supplementaryInformation.docx